

# Leman-Baikal Project

## Annual report 2015



ULM flying above Lake Baikal

Publisher: Ecole Polytechnique Fédérale de Lausanne, Limnology Center, CH-1015 Lausanne, 23 November 2015

Sponsored by:



Coordinated by: Limnology Center and



Consulat honoraire  
de la Fédération de Russie  
à Lausanne

# 1. Résumé

Le projet Léman-Baïkal a pour but de comparer le Lac Léman en Suisse et le Lac Baïkal en Russie, en développant une nouvelle plateforme de télédétection sur des ultra-léger motorisés (ULM). Les images hyperspectrales collectées permettront de cartographier l'hétérogénéité spatiale des propriétés de l'eau à une résolution spatiale et temporelle encore jamais obtenue.

Ce projet multidisciplinaire Suisse-Russe regroupe différents laboratoires de l'Ecole Polytechnique Fédérale de Lausanne et des équipes du « Baikal Institute for Nature Management » et « Lomonosov Moscow State University ». Quatre laboratoires de l'EPFL (TOPO, LASIG, APHYS, ECOL) se concentrent sur la télédétection pour créer des cartes de la chlorophylle a, la matière en suspension, le carbone organique dissous et la température à la surface des deux lacs. Deux laboratoires (EFLUM, CRYOS) en collaboration avec l'Université de Princeton étudient développent des capteurs de température et humidité ultra-rapides.

En 2015, les derniers vols sur le Lac Léman ont eu lieu d'avril à juin. Les vols se sont focalisés sur l'embouchure du Rhône, ou proche de Cully et de Morges. En général, trois vols par jour ont été effectués au même endroit à trois altitudes différentes. Cette stratégie devrait permettre de détecter des processus à court-terme, et de mieux interpréter les corrections atmosphériques.

En juillet – août 2015, nous avons organisé une campagne de terrain extensive autour du Lac Baïkal, où cinq sites ont été analysé en détail. Pour les trois premiers sites, la plateforme de télédétection a été montée sur un ULM, alors que les deux derniers sites ont été survolés par une caméra plus petite attachée sur un drone. Pour calibrer ces images, un grand effort de mesures in-situ sur le terrain a été accompli. Les différents types de phytoplancton ont également été analysés à la surface du lac, pour évaluer leur distinction potentielle par télédétection. Le succès de cette campagne a été assuré par la collaboration avec les chercheurs russes impliqués dans ce projet.

Le traitement de cette énorme quantité de données a bien progressé. Quatre étudiants Russes, Mikhail Tarasov, Galina Shinkareva, Tatiana Zengina and Tamir Boldanov, ont travaillé pendant un stage de 4 mois sur les images collectées sur le Delta du Selenga. Ils ont réussi à créer une carte des principales plantes du delta. De plus, un nouveau software HypnOS a été développé pour visualiser et corriger les images. Nous espérons donc que les résultats évalueront bientôt l'hétérogénéité de la qualité des eaux des deux lacs à une haute résolution spatiale et temporelle.

L'acquisition des données dans le projet Léman-Baïkal s'est achevée en 2015. Leurs interprétations et des publications sont attendues pour l'année prochaine.

## 2. Summary

The Lemman-Baikal project aims at comparing the water quality in Lakes Lemman in Switzerland and Lake Baikal in Russia, using a newly developed remote sensing platform mounted on ultralight aircrafts. The collected hyperspectral images will be used to map the spatial heterogeneity of water properties at a higher spatial and temporal resolution than ever achieved.

This Swiss-Russian multidisciplinary project regroups different laboratories within EPFL and teams from Baikal Institute for Nature Management and Lomonosov Moscow State University. Four EPFL laboratories (TOPO, LASIG, APHYS, ECOL) are focussing on remote sensing to map chlorophyll a, total suspended matter, dissolved organic carbon and temperature in surface water of both lakes. Two laboratories (EFLUM, CRYOS) in collaboration with Princeton University are developing ultra-fast temperature and humidity sensors.

In 2015, the last flights on Lake Geneva took place from April to June 2015. The flights focussed near the mouths of the Rhône River, near Cully and Morges. The same site was flown over three times a day at 3 different altitudes. This strategy should allow to detect processes at short-time scale, and also to better interpret the atmospheric correction.

In July-August 2015, we organized an extended field campaign over the entire Lake Baikal, where five sites were investigated in more details. On the first three sites, the remote sensing platform was mounted on a ULM, while the last two sites were investigated using a smaller camera mounted on a drone. To calibrate the collected images, a large effort for ground-truthing was accomplished. The different types of phytoplankton were also analysed in the surface water, to assess their potential distinctions by remote sensing. The success of this last campaign was ensured by the collaboration with Russian scientists implicated in the project.

Data processing of the massive dataset has greatly improved. Four Russian students, Mikhail Tarasov, Galina Shinkareva, Tatiana Zengina and Tamir Boldanov, worked on the data collected on the Selenga Delta during four-month internship. They created a map with the main vegetation types in the Selenga Delta. A new software HypnOS was developed to visualize and correct the images. We therefore expect that results will soon assess the heterogeneity of water quality on both lakes at a high spatial and temporal resolution.

Data acquisition within the project Lemman-Baikal was finalized in 2015, and data interpretation and publications will follow next year.

## Table of Content

1. Résumé .....	2
2. Summary .....	3
3. Remote sensing platform – TOPO / LASIG laboratory .....	5
3.1. Methodology .....	5
3.1.1. Objectives of TOPO laboratory within Project .....	5
3.1.2. Acquisition Process .....	5
3.2. Results from field Campaign 2014-2015 .....	6
3.2.1. Lake Geneva .....	6
3.2.2. Lake Baikal .....	6
3.3. Geometric Correction .....	9
3.4. Radiometric Correction .....	11
3.4.1. Atmospheric Correction .....	11
3.4.2. Other Issues .....	12
3.5. Data Visualization: the HypOS Software .....	13
3.6. Conclusion .....	15
4. Water Quality - Margaretha Kamprad Chair (APHYS) .....	16
4.1. Introduction and objectives .....	16
4.2. Material and method .....	16
4.2.1. Radiometric measurements .....	18
4.2.2. Optical properties .....	19
4.2.3. Biogeochemical measurements .....	20
4.2.4. Biological measurements .....	21
4.3. Results and discussion .....	21
4.4. Perspective .....	24
4.5. Conclusion .....	24
5. Surface Heat Flux Variability in a Large Lake – ECOL Laboratory .....	25
5.1. Introduction .....	25
5.2. Satellite data .....	25
5.3. Bulk modeling of SHF .....	27
5.4. Meso-scale LSWT data acquisition platform .....	31
5.5. Outlook .....	32
6. Princeton effort in collaboration with EFLUM/CRYOS .....	34
6.1. Objective .....	34
6.2. Sensor development .....	34
6.3. Field experiments .....	36
7. Reference .....	37

### **3. Remote sensing platform – TOPO / LASIG laboratory**

K Barbieux, Dr. Y Akhtman, D Constantin, Prof. F Golay and Prof. B Merminod.

#### **3.1. Methodology**

##### **3.1.1. Objectives of TOPO laboratory within Project**

The tasks of TOPO laboratory in the Lemman-Baikal project was to collect and process hyperspectral data, so that it can be used by scientific partners to perform image analysis.

We collected data using either:

(i) a hyperspectral system of our own, comprising a Headwall camera, mounted on a ultralight trike.

(ii) an OXI camera, designed by Gamaya, mounted on a drone.

Our role was then to process this data both geometrically and radiometrically, and make it accessible and usable for other labs.

##### **3.1.2. Acquisition Process**

Our hyperspectral system is composed of a Headwall Photonics pushbroom camera (250 bands), an RGB camera, a SGB-Systems Ekinox N navigation sensor, and a computer that interacts with the sensors (Figure 1).



Figure 1: our system contains a hyperspectral camera, an RGB camera, and navigation sensors to georeference the images.

The computer has an internal memory of 400 Gigabytes. During the flights, lines are acquired with a frequency of 50 Hz. The data is stored in the form of images which are concatenations of 1000 lines, in the .bil (Band Interleaved by Line) format. For each of them, a header file containing the orientation parameters for each line is generated thanks to the navigation sensors outputs. After the flights, data is transferred on our server. To visualize/process the data, we have designed a software called HypOS which is introduced in Section 6.

## **3.2. Results from field Campaign 2014-2015**

### **3.2.1. Lake Geneva**

During the months of September 2014, April and May 2015, 15 flights were performed over Lake Geneva. The map shown on Figure 2 summarizes the lines flown and gives an overview of the area covered.

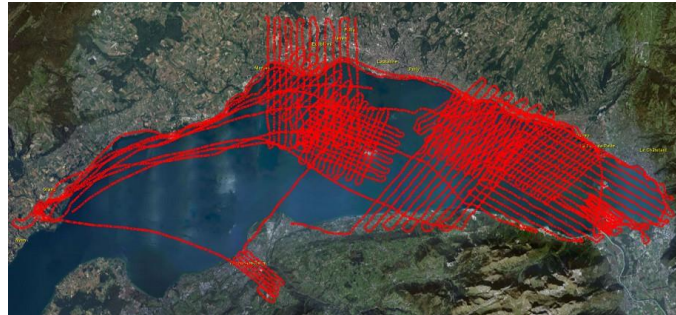


**Figure 2: lines flown over Lake Geneva between September 2014 and May 2015.**

As most of Lake Geneva had already been covered during previous years, the purposes of this year's flights were to cover the remaining areas as well as help to calibrate our sensors. Indeed, as shown on Figure 2, many flight lines overlap: these flights were actually performed at different altitudes to assess the influence of the atmosphere and the vehicle's orientation on our measurements. Therefore, the data will serve as a test case in a near future for our radiometric calibration process (presented in Section 3.4.2).

### **3.2.2. Lake Baikal**

In 2015, the acquisition campaign over Lake Baikal took place from 8<sup>th</sup> July to 14<sup>th</sup> August. While previous campaigns focused on the Selenga delta, we worked on 6 different sites this year: the delta, Turka area, Ust-Barguzin area, Monachovo Bay, Nizhneangarsk area and Olkhon. Figure 3 shows the location of the different sites.

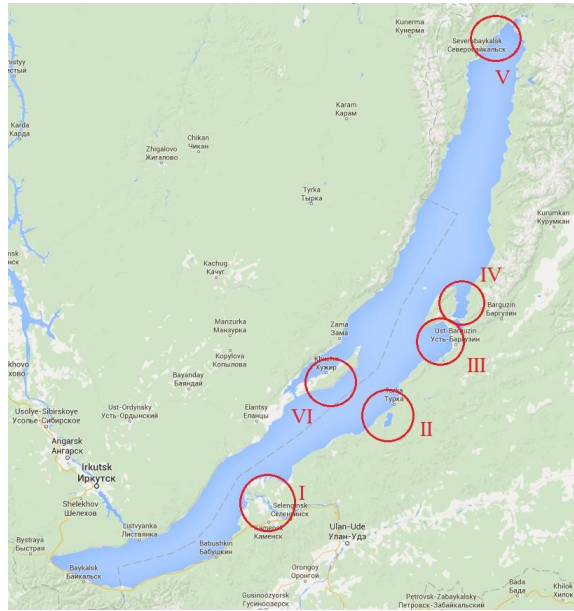


**Figure 3: the different sites explored during our summer campaign. I: Selenga delta; II: Turka/Lake Kotokel; III: Ust-Barguzin; IV: Monachovo Bay; V: Nizhneangarsk; VI: Olkhon.**

Our two objectives in the Selenga delta were to cover areas that had not been covered yet during previous campaigns, and synchronize with the team from Moscow State University (MSU) to collect data from the same ground control points with an Ocean Optics Spectrometer. Figure 4 shows the flights realized during the first week of the campaign.

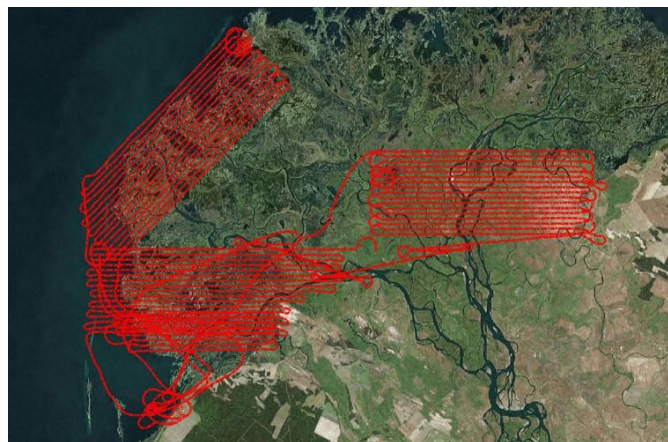


**Figure 4: flight lines crossed by the ultralight over the Selenga delta in 2015.**

The Limnology lab of EPFL joined us at the second site (Turka). The main goals there were to collect data at points of interest for the Limnology Lab, and acquire data over the whole Lake Kotokel for MSU. Figure 5 illustrates our work.





**Figure 5: flight lines crossed by the ultralight over Turka**

Data from both Selenga delta and Lake Kotokel were processed. Data from the delta is already used by MSU. Among the rest of the data, one part is used for calibration purposes (see Section 3.4.2), and the other part is reference data to test this calibration process. Once the calibration is validated, the images will be used by APHYS laboratory to study Lake Baikal waters, also in Ust-Barguzin area (shown on Figure 6).



**Figure 6: flight lines crossed by the ultralight over Ust-Barguzin.**

Due to bad weather conditions (especially wind conditions), Monachovo Bay could not be surveyed. Four short drone flights (about 30 km each) were performed on the last two sites (Nizhneangarsk and Olkhon). Since it was the first time that an OXI camera was used for collecting data from Lake Baikal, the results have to be studied



carefully to assess the performance of the camera and the possibility of using it again in the future. Data from this camera will be analyzed later.

### **3.3. Geometric Correction**

Great progress were made recently on geometric correction. The "raw" orthorectification, using the orientation parameters output by our navigation sensors, was not sufficient to provide correct and consistent georeferencing of the data. This issue is now solved.

The RGB images acquired simultaneously to the hyperspectral lines are processed by bundle adjustment techniques (Triggs and al. 2000), which allows to retrieve better orientation parameters for each image. The closest pushbroom line (in time) is given this orientation. Multiple lines are corrected that way, and the parameters for the rest of the lines are computed by interpolation. Figure 7 shows an example of improvement realized thanks to this technique.

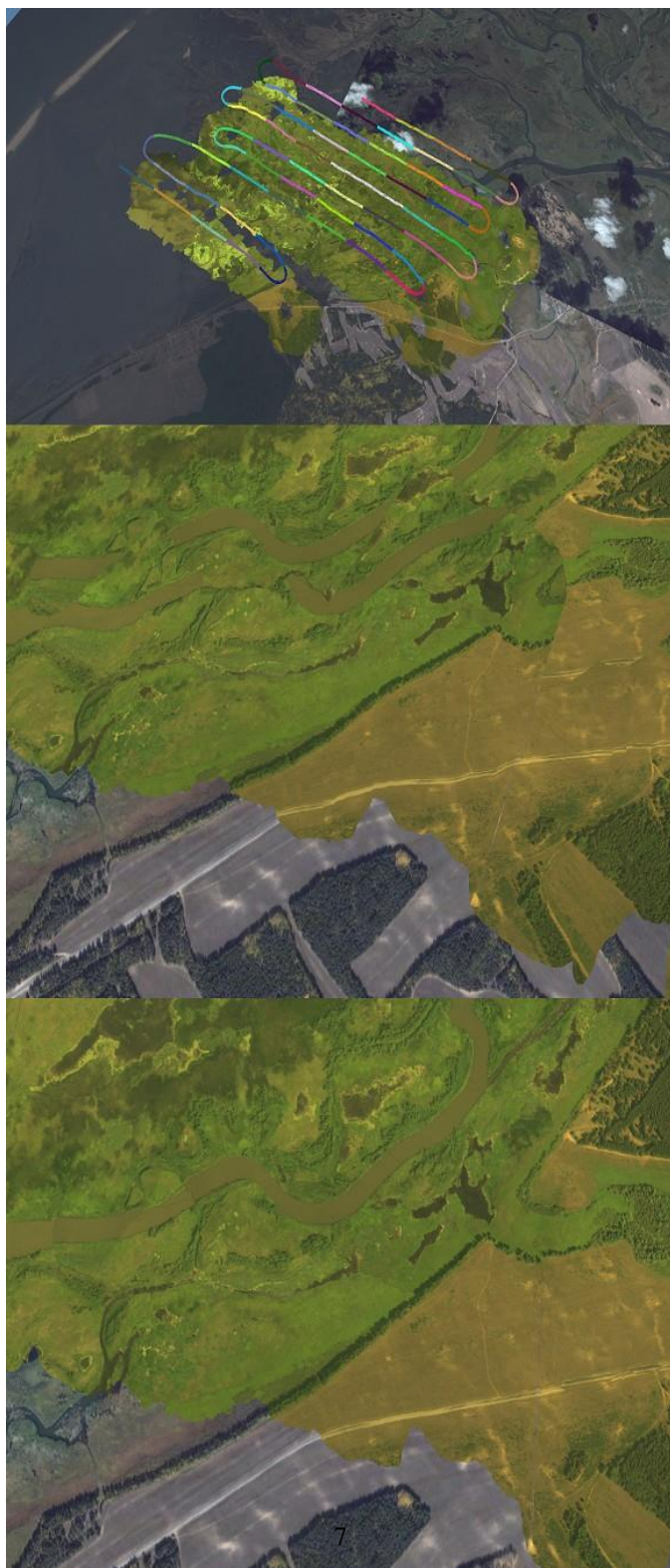


Figure 7: flight path (top) and extract from the projection before (middle) and after (bottom) correction, for a flight over the Selenga delta.

Three sample flights performed at different altitudes were corrected using this method. The results are summarized in Table 1.

	Mean Elevation [m]	Mean Residual Before Correction [m]	Mean Residual After Correction [m]
Flight 1	500	13.8	6.1
Flight 2	1000	49.2	8.0
Flight 3	1500	46.3	10.5

**Table 1: comparison of mean residual before and after correction for 3 flights of different altitudes.**

Two ideas have been explored to further refine the precision of the georeferencing. The first one is a better synchronization between the RGB camera and the hyperspectral, to make sure the orientation parameters output by the bundle adjustment are given to the right pushbroom line. The second one is to improve our filtering of the navigation data. It is currently processed by a Kalman filter directly inside the sensor. Extra filtering could allow to get better orientation parameters before the bundle adjustment is performed. It is critical to explore these ideas as the current algorithm highly relies on the presence of salient elements inside the images. Thus, plain surfaces like water are hard to process when they are not surrounded by land.

An article about geometric correction, entitled "Geometric Correction for Airborne Hyperspectral Imagery", will be submitted to ISPRS 2016.

### **3.4. Radiometric Correction**

The data we collect has to be processed to account for several problems.

#### **3.4.1. Atmospheric Correction**

The first issue is the atmospheric absorption: some radiations are absorbed by the atmosphere, thus inducing artefacts in our raw data. Figure 8 shows an example of such problem.

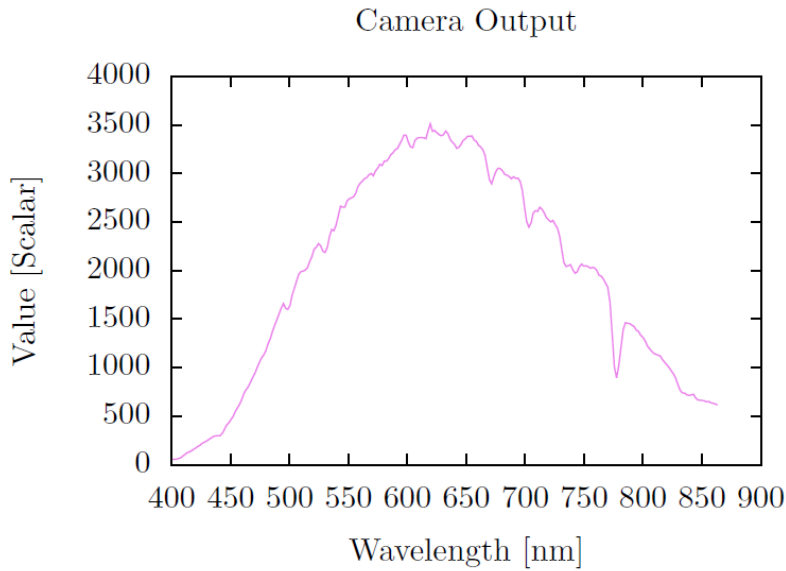


**Figure 8: Typical output spectrum from our camera. Down peaks corresponding to absorbed radiations can be observed; the most noticeable, around 780 nm, is due to water vapor in the atmosphere.**

In 2015, TOPO laboratory managed to develop an algorithm that tackles this issue. Assuming reasonable smoothness of the spectra, the raw data can be corrected to remove these atmospheric effects. This method, called Smoothing Technique for Empirical Atmospheric Correction (STEAC), performs better than other methods. A paper (Manuel Cubero-Castan et al. 2015) was published in the WHISPERS 2015 conference, and a second one ("Irradiance Fitting Atmospheric Correction - a Novel Atmospheric Correction Algorithm using Illuminant Spectral Fitting.") was submitted to IEEE Journal of Selected Topics in Applied Earth Observations and Remote Sensing (JSTARS 2015).

### 3.4.2. Other Issues

Other problems include: non uniform sun intensity within flights; moving mechanical elements inside our sensors, which shift the signals on the wavelengths axis; noise inside the signals. A paper entitled "Computation and Storage of Calibration for Airborne Hyperspectral Sensors", which explains how we deal with all these problems, was submitted to JSTARS 2015. Figure 9 shows a comparison between a processed signal from our camera and the ground truth acquired by APHYS laboratory of EPFL using an Ocean Optics Spectrometer.

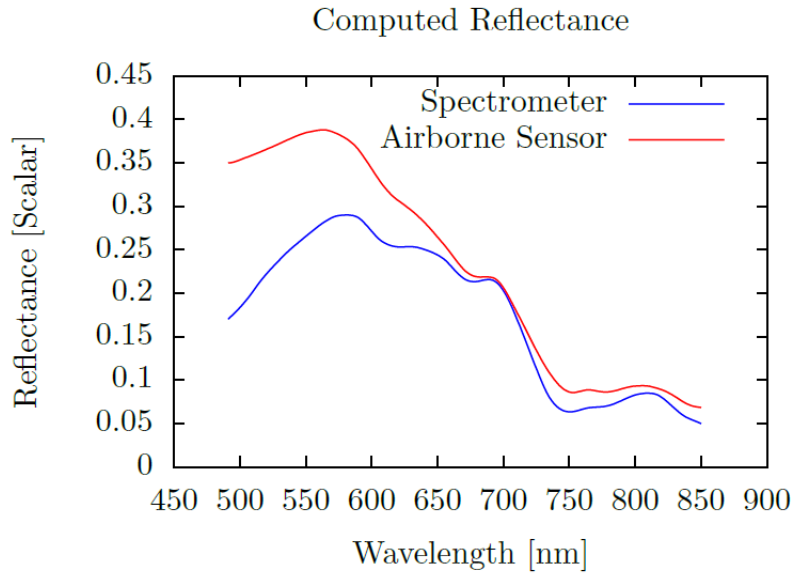


Figure 9: Outputs of the spectrometer and the hyperspectral camera.

### 3.5. Data Visualization: the HypOS Software

To enable the visualization and the use of the hyperspectral data, we provide scientific partners with a software called Hyperspectral Orthorectification Software (HypOS). It is a geographic information system based on NASA Worldwind SDK where pushbroom hyperspectral data in the .bil format can be imported, georeferenced and processed.

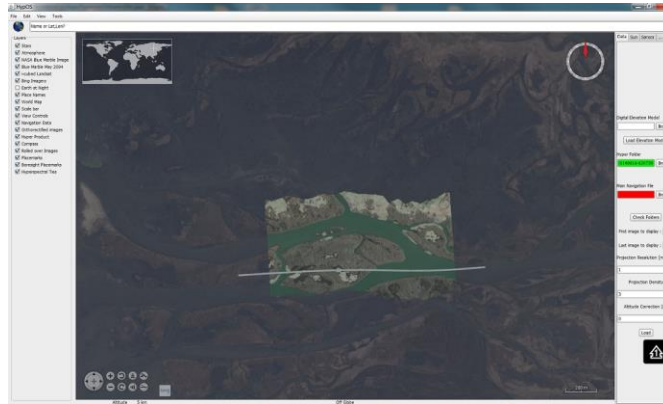


Figure 10: HypOS software.

The software provides all the features necessary to obtain relevant hyperspectral information: uniformization of light intensity (to account for the varying sun

conditions within one flight), geometric and radiometric correction for the data, and exportation of areas of interest into .bil files.



**Figure 11: example of light intensity correction: top image represents a flight visualized in HypOS before correction, and bottom image illustrates the same after correction.**

In 2015, all these features were successfully implemented. This software is already actively used by MSU to process images of interest: one paper about the classification of these images was already published (Tarasov et al. 2015). New possibilities were constantly added. A single problem remains: the software demands high computer performances to work properly (64 GB of RAM are sometimes not enough to process large-scale flights), and the current radiometric correction is slow (depending on the computer performances, one to several hours to compute smooth spectra). The current work on the software aims at reducing the RAM necessary to run it, and increase the processing speed.

### **3.6. Conclusion**

During the academic year 2014-2015, TOPO has solved most of the issues related to its work for the Lemna-Baikal project. Firstly, an atmospheric correction algorithm independent of any calibration data was developed, and should allow us to process data from the 2013 campaign in a near future. Secondly, an entire calibration process has been designed to correct data from 2014 and 2015 radiometrically. This calibration was implemented and should be usable, through the HypOS interface, to scientific partners in a near future. Thirdly, a new geometric correction algorithm allowed us to correct the navigation parameters of all the data acquired so far. The results are hyperspectral lines that are much better georeferenced. Finally, the development on HypOS is still ongoing. It is ready for use for other labs. The current work aims at improving the overall processing speed of the software, which is currently slow for large-scale studies. Part of the work has already been published, is under review (in JSTARS 2015) or will be submitted to upcoming conferences (ISPRS).

Our future work is divided in three tasks. The first one, as already mentioned, relates to the usability of HypOS. The second one consists in making the processed data of all campaigns available for other labs. Concretely, for each lake, a map matching each area to a flight should be accessible, so that each scientist involved in the project can easily find the data he/she is interested in. The data that has not been processed geometrically/radiometrically will be processed. The third task is a theoretical work aiming at improving the geometric correction for plain surfaces like water. Current methods are satisfying but demand that part of the flights is performed over land. We will investigate how it is possible to remove this constraint.



## **4. Water Quality - Margaretha Kamprad Chair (APHYS)**

### **4.1. Introduction and objectives**

Each substance has a unique color associated with its absorption, scattering and/or light transmission. Interpretation of the Remote Sensing signal acquired from an airborne or spaceborne sensor is therefore inherently depending on the type of substances and organisms in the water and their associated optical properties (i.e. how they interact with the light). Our research is in the earth of this booming technology and aim at referencing the optical properties of two major lakes in Western Europe and Eastern Russia, Lake Geneva and Lake Baikal. The first outcome of our activity is to provide the required dataset for accurate estimation of biogeochemical substances and possibly different phytoplankton communities over the entire lake from remote observations with future sensors like OLCI (ESA) on Sentinel-3 and hyperspectral ultra-light sensors like the one developed within this project. More fundamentally, our research will allow to validate and interpret Remote Observations above Lake Baikal and Lake Geneva by providing Inherent Optical Properties (IOPs) coefficients and algorithm recommendations for multi to hyperspectral sensors. Of particular importance is the relation between the vertical structures of the water constituents' IOPs and the Reflectance measured above the water. In this report we present three principal structure of vertical stratification: (i) Concentrations decreasing with depth; (ii) Gaussian-like profile with maximum concentration a few meters from the surface and (iii) constant concentration within the light penetration depth.

### **4.2. Material and method**

During a circum-Baikal cruise in summer 2015, 77 sites all over Lake Baikal (Figure 12) where sampled. Data over Lake Geneva (Figure 13) were sampled over 64 sites between spring and summer. In order to link the biogeochemical content with the lake color as observed from the sky or from space, different types of measurements are required. By color we mean the ratio between incoming light from the sun and the light exiting the water which is commonly called reflectance.

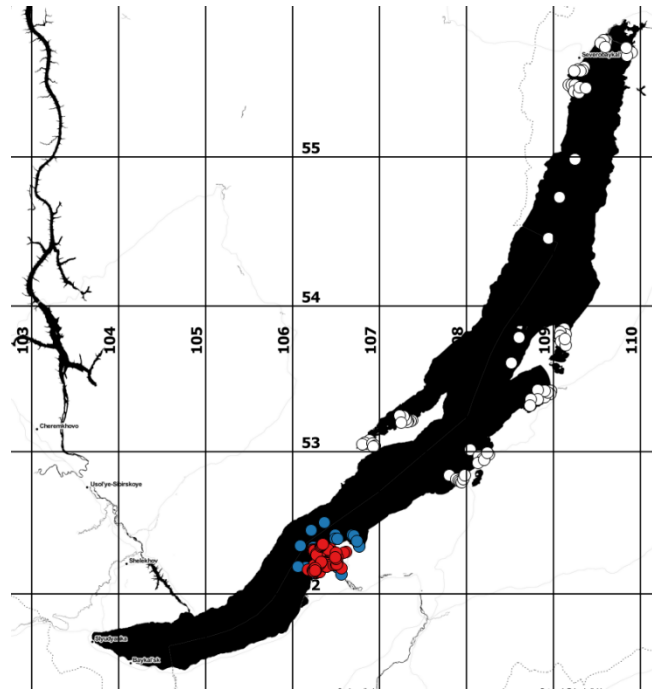


Figure 12: Lake Baikal ground control locations sampled in 2015 (White), 2014 (Red) and 2013 (Blue).

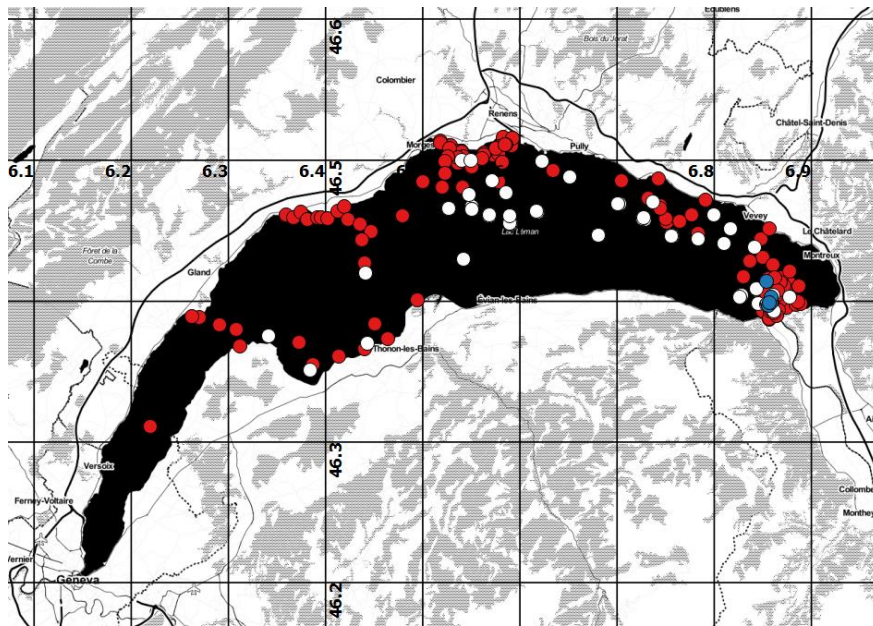


Figure 13: Lake Geneva ground control locations sampled in 2015 (White), 2014 (Red) and 2013 (Blue).

Figure 14 shows the locations of the stations that will be presented in the following section. These sites illustrate the three main vertical structures we proposed for this study in introduction. Four kinds of measurements were performed on-ground, and will be described in the following section.

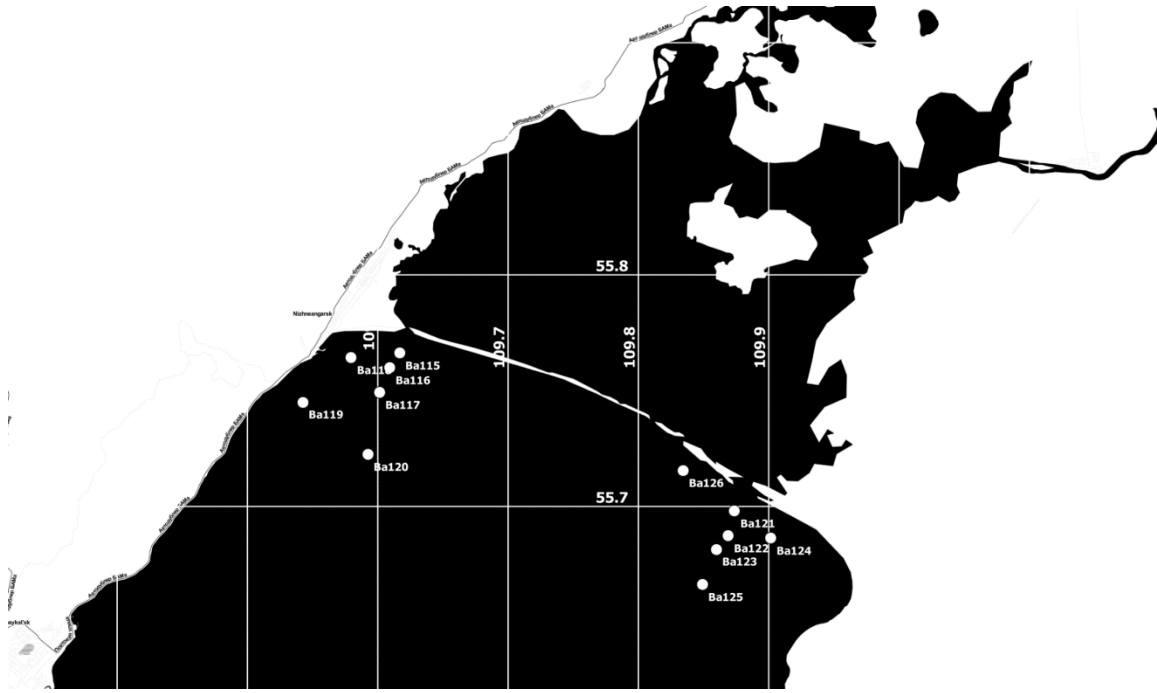


Figure 14: Northern part of Lake Baikal with sampling stations corresponding to the examples shown in this section. Sampling dates are 30.07.2015 (Ba115-118) and 31.07.2015 (Ba119-126).

#### 4.2.1. Radiometric measurements

Radiometers used in this study are hyperspectral in-situ radiometers with spectral resolutions  $< 4\text{nm}$  in the visible domain (400-850nm). Namely, we used an Ocean Optics USB2000+, a TriOS Ramses, and Water Insight WISP-3. These measurements serve three main purpose: (i) they allow the simulation of a large dataset using radiative transfer models; (ii) the generated dataset is used to create a model adapted to the particular water composition observed; (iii) they allow to validate the remote observations and the atmospheric correction. For instance, the ULM used in this study were flying at an altitude of 1km where the atmospheric contribution is significant, and thus the reflectance observed from the later platform has to match the reflectance observed on the ground.

Validation activities in inland waters are principally performed using different systems either deployed above- or in-water. In the following we focus on in-water measurements from the Ramses at a minimum of three depths ( $z$ ) but all quantities measured are given in Table 2.

Symbol	Definition	Unit	Instruments
$E_d^-, E_u^-$	Down- and upwelling irradiance below the surface	$W.m^{-2}$	Ramses
$E_d^+$	Downwelling irradiance above the surface	$W.m^{-2}$	WISP-3, USB2000+
$L_u^-$	Upwelling radiance below the surface	$W.m^{-2}.sr^{-1}$	Ramses
$L_w$	Water leaving radiance	$W.m^{-2}.sr^{-1}$	Ramses
$K_d, K_u, K_l$	Down-, upwelling and diffuse attenuation coefficients	$m^{-1}$	Ramses
$R_{rs}^+$	Remote sensing reflectance above the surface	$sr^{-1}$	Ramses, WISP-3, USB2000+
$R_0^-$	Irradiance reflectance just below the surface ( $z = 0$ )	No unit	Ramses, WISP-3

Table 2: definition of key terms

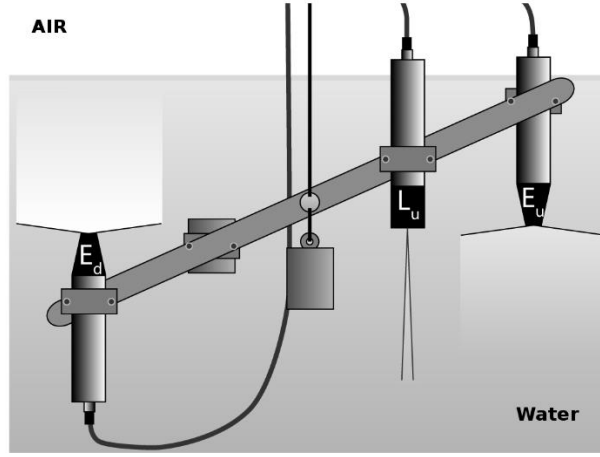


Figure 15: TriOS Ramses configuration used in this study. The three quantities measured are  $E_d^-$ ,  $E_u^-$ , and  $L_u^-$

Figure 15 depicts the Ramses configuration. The sensor with a field of view measure the radiant energy in one direction. This quantity is called the upwelling radiance ( $L_u^-$ ) with superscript '-' indicating in-water measurement. The other two sensors measure the downwelling and upwelling irradiance ( $E_d^-$ ,  $E_u^-$ ) corresponding to hemispherical integral of the incoming light. These quantities allow us to calculate the diffuse attenuation coefficients  $K_l$ ,  $K_d$  and  $K_u$  using linear polynomial fits over a n-depth profile of  $\ln(L_u^-)$ ,  $\ln(E_d^-)$  and  $\ln(E_u^-)$  respectively. Values of  $L_u(0^-)$ ,  $E_d(0^-)$  and  $E_u(0^-)$  just below the surface are the intercepts of the best fit line passing through the n depth profiles and the 0 depth. The latter two quantities are used to calculate the Irradiance reflectance ( $R_0^-$ ) as in:

$$R(0^-) = \frac{E_u(0^-)}{E_d(0^-)} \quad (1)$$

To account for the air-sea interface effects,  $L_u^+$  and  $E_d^+$  are extrapolated through the surface to give  $L_w(\lambda)$  as in:

$$L_w(\lambda) = L_u(0^-, \lambda) \frac{[1-\rho_f]}{n^2} \quad (2)$$

Where  $\rho_f$  is the Fresnel reflectance of the sea-air interface, and n is the refractive index of seawater with an approximated value of 1.34.  $\lambda$  is used to account for all wavelength in the visible domain. The transmittance at the air-sea interface corresponding to the fraction on the right hand side of Eq. (2) is taken from well-established parameter and equal to 0.543. And  $E_d^+$  as in:

$$E_d(0^+, \lambda) = \frac{E_d(0^-, \lambda)}{1-\alpha} \quad (3)$$

Where  $\alpha$  is the Fresnel reflection albedo for irradiance from sun and sky (0.043).

Equations (2) and (3) allow us to calculate a second reflectance commonly used to account for directional effects as in:

$$R_{rs}^+(\lambda) = \frac{L_w(\lambda)}{E_d(0^+, \lambda)} \quad (4)$$

#### 4.2.2. Optical properties

When a light beam passes through a volume of water, part of the incident power is absorbed within the volume of water. Part is scattered out of the beam at different angles and the remaining power is transmitted through the volume with no change in direction. The sum of absorption and scattering within a volume is called the beam attenuation coefficient which can be directly measured with a transmissiometer or estimated from in-water radiometric profiles (Ramses measurements). Furthermore, absorption and scattering are a sum of contribution from various constituents. For instance, different phytoplankton communities will absorb different wavelength with diverse efficiency and different size/composition of particles will scatter light more or less efficiently (see Figure 16).

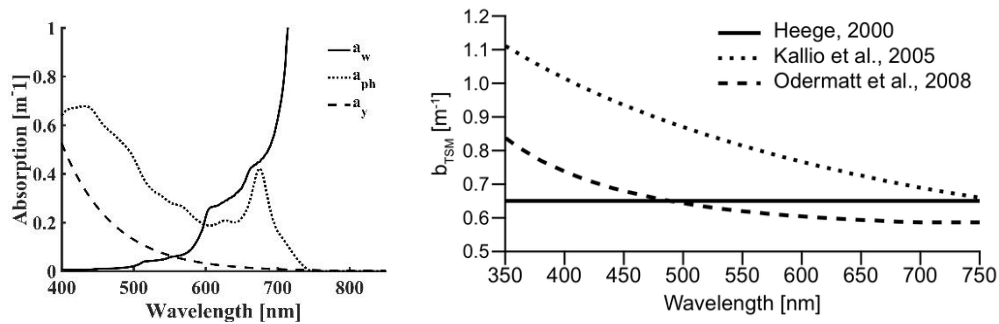


**Figure 16: (Left) Absorption by the main contributors in natural waters. Subscript 'w' stands for water, 'ph' stands for a classical phytoplankton specie and 'y' stands for yellow substances (colored dissolved organic matter). (Right) scattering according to several authors.**

In collaboration with P. Hunter from the University of Stirling a complete set of IOPs was measured in Lake Geneva using instruments mounted on a cage including a Wet Labs ac-9 to measure absorption at 9 wavelengths in the water column. Several filters were used on the ac-9 to separate organic, inorganic and dissolved substances. The backscattering was measured using a Wet Labs bb-3 at 3 angles. In Lake Baikal only the bb-3 was used, and Colored Dissolved Organic Matter (CDOM) absorption was measured using photometry in collaboration with Tom Battin from SBER laboratory at EPFL.

#### 4.2.3. Biogeochemical measurements

Biogeochemical measurements were performed using a Wet Labs ECO-FLS fluorimeter and a Wet Labs C-Star transmissiometer mounted on a SeaBird CTD 19+V2, and a Sequoia LISST-100X. They were used to measure chlorophyll-a (Chl-a), turbidity from beam attenuation and particle size distribution, respectively. In Lake Baikal we used a Sea & Sun CTD with a similar fluorimeter but a turbidimeter instead of the transmissiometer allowing to measure only turbidity. Finally, the water analysis included laboratory estimation of Chl-a, Total Suspend Matter (TSM), and Dissolved Organic Carbon (DOC – related to CDOM absorption). As illustrated in Figure 17, water sampling was used to calibrate the fluorimeter and the transmissiometer/turbidimeter.

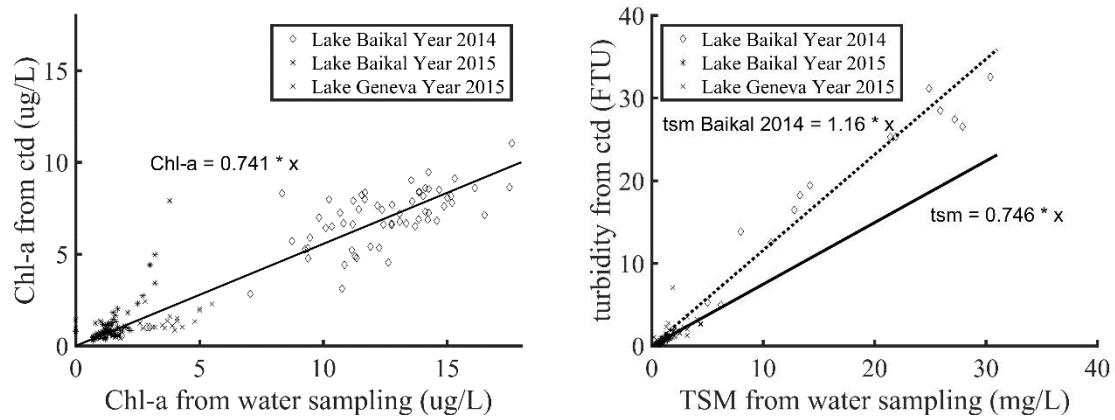


**Figure 17: Linear regression between water sampling and the Sea Sun CTD measurements of (left) Chlorophyll-a against fluorescence and (right) TSM against turbidity – we note here that two regressions were performed, one for Lake Baikal 2014 dataset and one for the rest.**

Along with Chl-a analysis, water samples were acquired at every locations and prepared for High Performance Liquid Chromatography (HPLC) analysis. HPLC will allow the detection and quantification of other pigments like Phycocyanin which is specific to cyanobacteria. In addition, the University of Irkutsk gathered a dataset of Chlorophyll and particle all around the lake almost every summer since 70 years. This dataset will allow to evaluate the temporal representativeness of our study by applying the optical properties we will define to remote observations in the past like those from MERIS sensor (ESA).

#### 4.2.4. Biological measurements

During 2015 cruise on Lake Baikal, University of Irkutsk collected water samples at the same location, to identify and count the different phytoplankton species in the surface water. The identification will allow to elaborate a bio-ecological model, in order to interpret the pigment retrieved like Chlorophyll-a into phytoplankton biomass.

### 4.3. Results and discussion

In the following section, we present the results obtained at three selected sites corresponding to the three stratification cases mentioned previously. As depicted in Figure 18 below, at site Ba118 concentrations were decreasing with depth from 10  $\mu\text{g/L}$  at the surface to 3  $\mu\text{g/L}$  at 9 m for Chl-a and from 1.8 mg/L to 0.4 mg/L for TSM. At site Ba119, the Chl-a profile has a Gaussian shape with a maximum around 1.5 meter depth of 12  $\mu\text{g/L}$  and a minimum of 2.4  $\mu\text{g/L}$ . The TSM profile at this site is almost constant with an average value of 0.8 mg/L. At site Ba120 we observed constant concentration of photo-active substances with depth for both substances with value slightly varying around 4.5  $\mu\text{g/L}$  and 0.3 mg/L for Chl-a and TSM respectively. At all sites the integral of Chlorophyll-a over the first 10 m of the water column were close to 5  $\mu\text{g/L}$ , TSM was equivalent between Ba118 and Ba199 with a value around 0.9 mg/L, and lower at Ba120. The CDOM absorption measured is  $> 1 \text{ m}^{-1}$  at sites Ba118, and close to  $0.5 \text{ m}^{-1}$  at Ba119 and Ba120. The horizontal lines on Figure 18 represent the Secchi depth measured at every site.

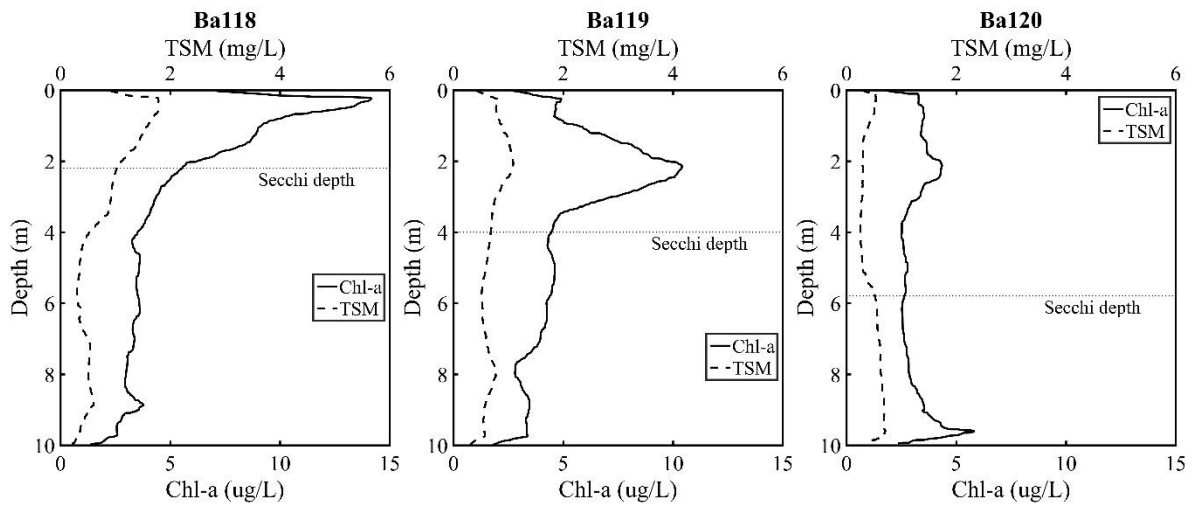


**Figure 18: CTD Sea & Sun calibrated profiles of the Chlorophyll-a and the Total Suspended Matter at sites Ba118, Ba119 and Ba123.**

In-water radiometers measurements (Ramses) are shown in Figure 19. They correspond to the estimated Irradiance reflectance just below the water surface. The three sites illustrates well the variability we can observe over short spatial distance. The region from 400 nm to 550nm illustrate the CDOM absorption effect which is the most important at Ba118 and the lowest at Ba120 where higher reflectance is observed. The particle concentration plays an important role in this region as well but its effect is clearer from 550 nm to 850 nm where most scattering (higher reflectance) happens at site Ba118 and Ba119. Because of the mixed contributions in the blue part of the spectra, the absorption peak of Chl-a used for the identification of phytoplankton in lakes is the one at 665 nm in the red. On all spectra we see a deep trough in this region followed by a peak due to the Chl-a fluorescence. From Figure 7 we saw that the integral of Chlorophyll-a especially and particles to some extent over the first 10 meters of the water column are equivalent but we see differences on the estimated Irradiance reflectance in Figure 19 due to the vertical shape of the concentrations. The first step to evaluate these differences is to check the quality of the estimation.

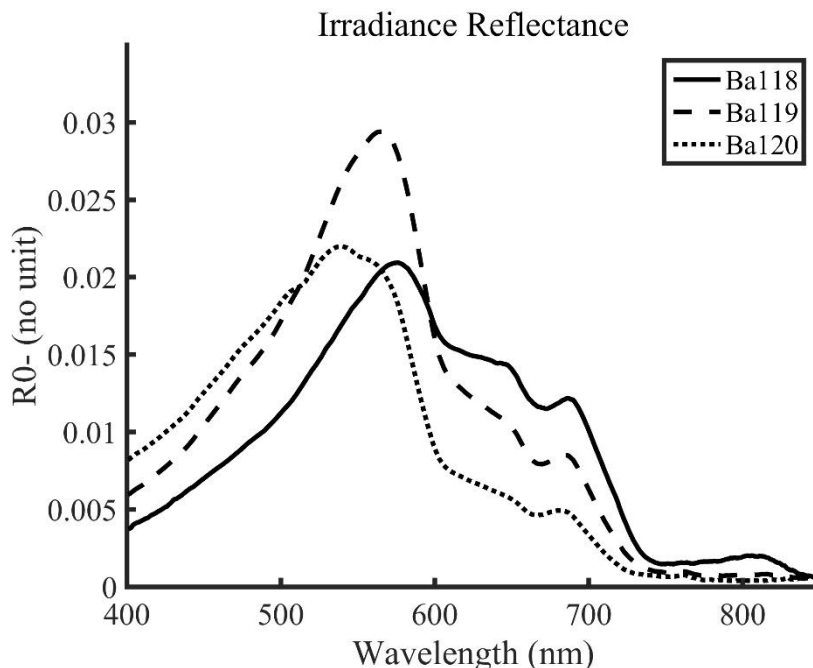


**Figure 19: Irradiance reflectance under the surface (R0-) at three stations shown in Figure 12.**



Preliminary data quality check is performed using the Water Color Simulator (WASI) which is a software tool for analyzing and simulating the most common types of spectra that are measured by ship-borne optical instruments. Basis of all calculations are analytical models with parameters well established among the community. From built-in absorption and scattering profiles, it allows us to set the Chlorophyll-a, TSM content and CDOM absorption of a water body to simulate the corresponding reflectance which is compared to the radiometric measurements in the Figure 20 below.

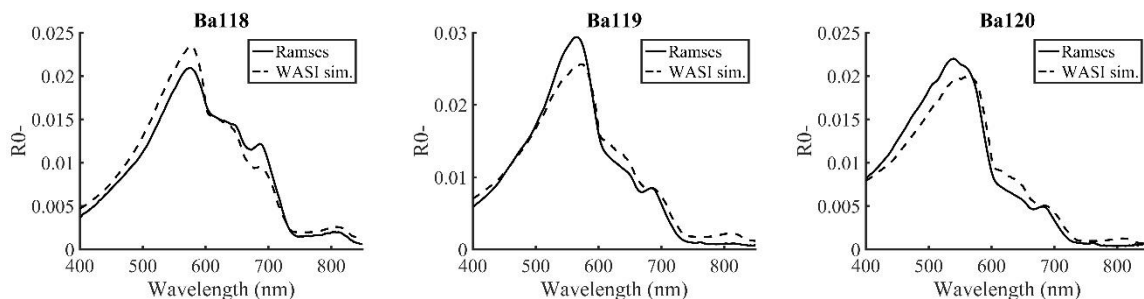


**Figure 20: Irradiance reflectance measured from the Ramses radiometer (solid line) and from WASI simulations (dotted line) at stations (left) Ba118 with Chl-a of 7  $\mu\text{g/L}$ , TSM of 1.2 mg/L and high CDOM; (middle) Ba119 with Chl-a of 6  $\mu\text{g/L}$ , TSM of 0.8 mg/L and lower CDOM; and (right) Ba123 with Chl-a of 2.5  $\mu\text{g/L}$ , TSM of 0.5 mg/L and low CDOM;**

Figure 20 shows that the CDOM absorption and particle scattering part of the spectra fits well with WASI simulations. However, for Chl-a, we notice significant differences between the simulations and the Ramses measurements. This suggests that the built-in absorption spectra for Chl-a is not suitable for the Baikal waters and a more advanced tool need to be used for the simulation. The next step is thus to estimate the absorption by phytoplankton from the different measurements performed in Lake Baikal and to input the estimated coefficient into the simulation to be able to predict the reflectance for a given set of biogeochemical set of parameters.

One of the main goal of this study is to be able to use airborne or spaceborne observations to produce particle and Chl-a maps of the observed area. In order to have a glance at the outcomes of this study, we developed a model based on ground truthing measurements using empirical relationship with the ULM hyperspectral data from last year campaign over the Selenga region in Lake Baikal. In Figure 21 the model was applied to the ULM acquisition from 17<sup>th</sup> August 2014 on the North-Eastern part of the delta.

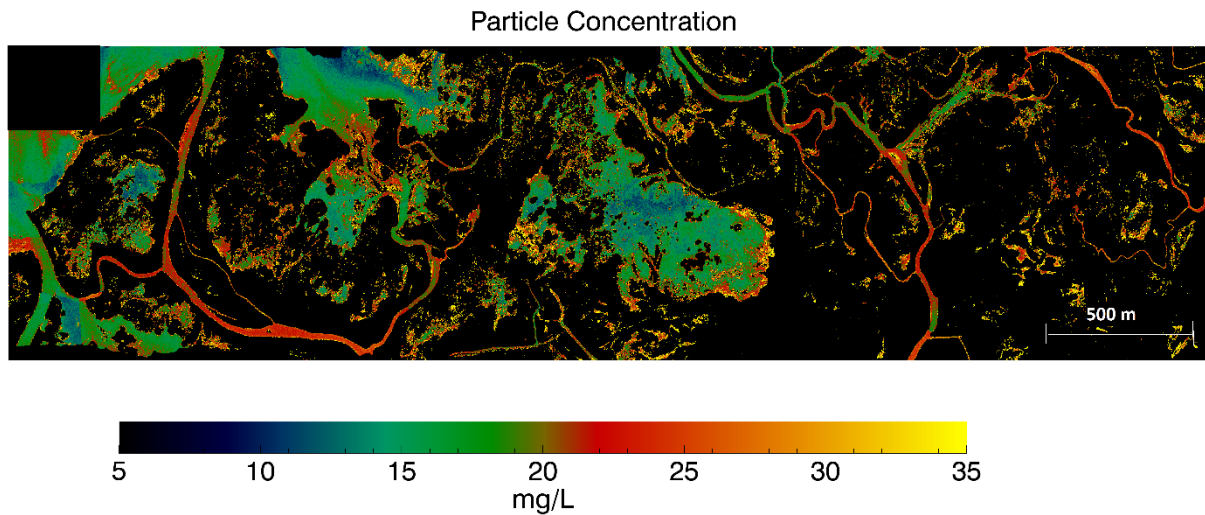


Figure 211: Particle map of the north-eastern part of the Selenga Delta. The image was acquired from the ULM flying at an altitude of 1 km above the delta on 17<sup>th</sup> August 2014.

#### 4.4. Perspective

The main steps for the coming year are:

- Effect of the stratification on radiometric measurements above and in-water.
- Estimation of the Optical properties of the water.
- Simulation of the different observed water types.
- Algorithm choice and evaluation.
- Sensitivity analysis.
- Interpretation of previous remote observations and ULM acquisitions.
- Publication of optical parameters and case studies.

#### 4.5. Conclusion

Lake Geneva is the largest freshwater resource of Western Europe and Lake Baikal the largest freshwater resource on earth. The evolution of their water quality is critical for drinking and domestic use, fisheries, agriculture, industries and recreational activities. The aim of the research is to allow a synoptic analysis of both lakes water quality and their evolution through historical, current and future remote sensors. We will focus on understanding the relation between the superficial layer stratification and the observed above-surface reflectance. In the previous years, we evaluated the capability of the hyperspectral sensors on the ULM, to accurately retrieve the bio-chemical parameters of specific regions and their short-term temporal evolution. We will extend this analysis to the entire lakes and the whole set of water-dedicated remote instruments available.

## **5. Surface Heat Flux Variability in a Large Lake – ECOL Laboratory**

Prof. D A Barry, A Irani Rahaghi

### **5.1. Introduction**

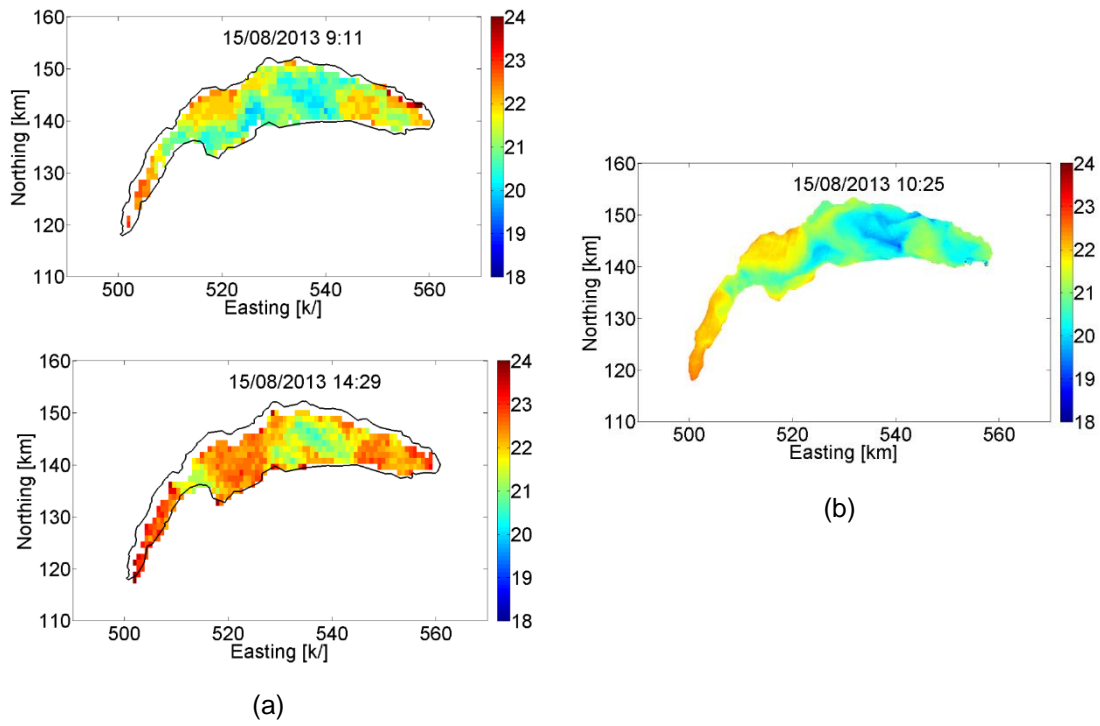
The net surface heat flux (SHF) along with the wind forcing are the main external forces affecting lake status. The SHF and indeed the entire lake ecosystem is influenced by the lake surface water temperature (LSWT). LSWT, which may spatially and temporarily vary over the lake surface, reflects meteorological and climatological forcing more than any other physical lake parameter. The objectives of the ECOL laboratory are: first, to identify the variability of the LSWT, and second, to characterize the main factors driving such variability. The availability of suitable data makes Lake Geneva an ideal site for investigating surface heat flux of a large lake.

This investigation uses available data, field measurements and a validated 3D hydrodynamic model (Delft3D). In this study, remotely sensed LSWT data including Advanced Very High Resolution Radiometer (AVHRR) and Landsat 8 satellite images, as well as a Balloon Launched Imaging and Monitoring Platform (BLIMP), which is used to measure the LSWT at meso-scale, are used. Furthermore, an operational numerical weather prediction model (COSMO-2, Swiss meteorological service), provides the spatio-temporal variability of meteorological data over Lake Geneva. Here, we also report on an investigation for estimating the Lake Geneva SHF by using AVHRR, COSMO-2 and the measured regular vertical temperature profiles at two points in the lake.

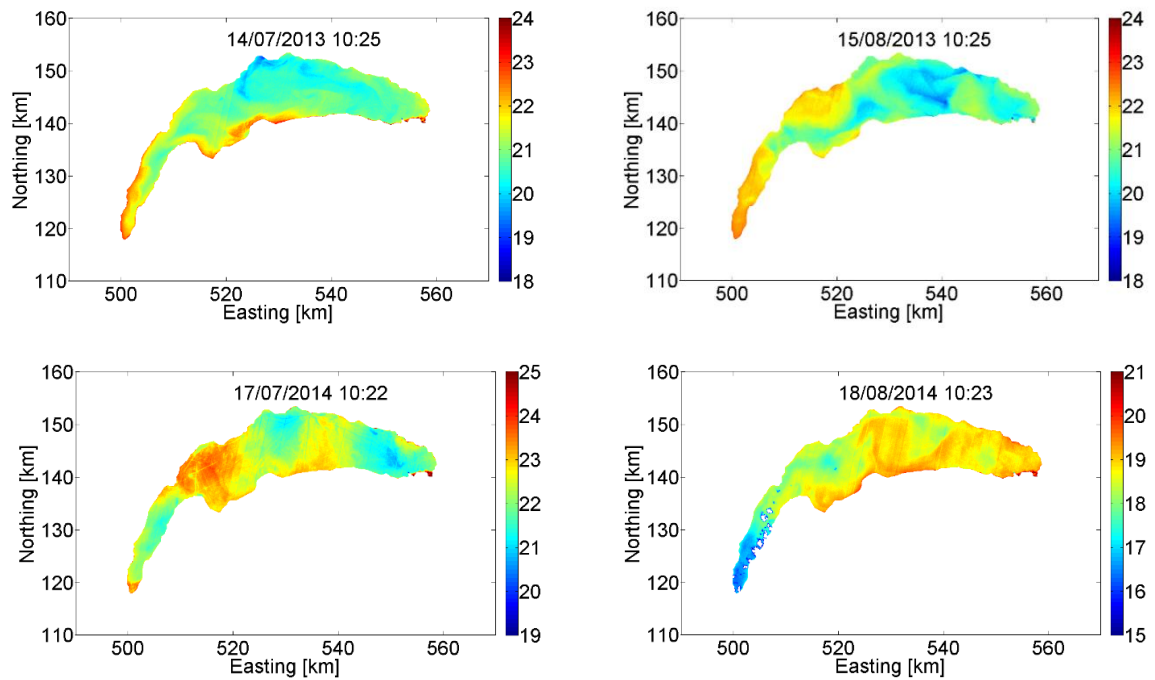
### **5.2. Satellite data**

We use two types of satellite thermal images. AVHRR data from the US National Oceanic and Atmospheric Administration (NOAA) have a spatial resolution of about 1 km x 1 km. We also retrieve Landsat 8 high-resolution thermal images. Its thermal bands are useful in providing more accurate surface temperatures, which are collected at a resolution of 100 m (resampled to 30 m in the delivered data product). The AVHRR data dates back to 1989 and Landsat 8 images to 2013 (Figure 22). Data in Figure 22 are for the same day but at different overpassing times. This figure reveals that the two datasets are in good agreement.

Landsat 8 provides higher resolution images and consequently a better indication of LSWT patchiness. However, the imaging frequency is every 16 days which makes it unsuitable for a statistical analysis. This dataset however provides a comparison tool for meso-scale data collected via a balloon or small aircraft, and local in-situ data collected via the ECOL autonomous catamaran (see Léman-Baikal annual report 2014). The summer time images, for example, suggest a variability of LSWT of about 5-6 °C over the entire lake (Figure 23).



**Figure 22: Examples of LSWT satellite data on 15<sup>th</sup> August 2015, (a) AVHRR at 9:11' and 14:29', (b) Landsat 8 at 10:25'.**



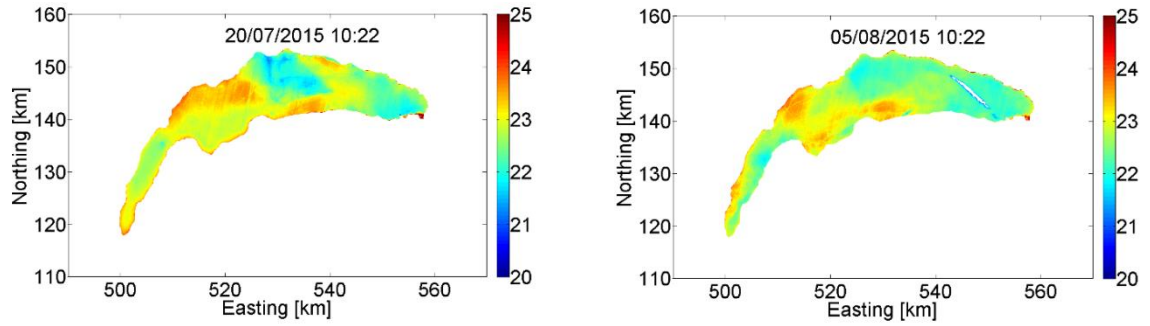


**Figure 23: Examples of Landsat 8 summertime LSWT data for 2013-2015.**

AVHRR images, on the other hand, are more frequent but with lower spatial resolution. Such images are used to estimate the seasonally temperature variability over Lake Geneva (Figure 24). A more detailed analysis of the SHF variability is illustrated in the next section.

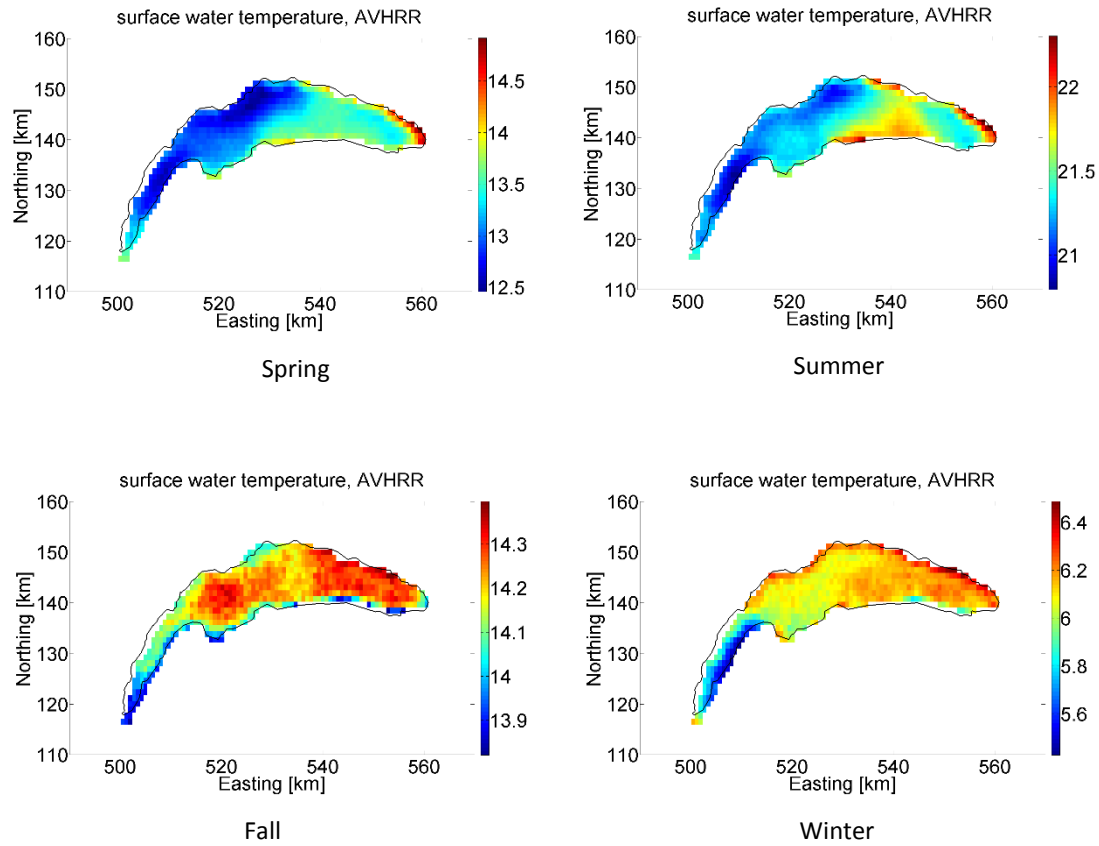


**Figure 24: Seasonal spatial patterns of LSWT by using AVHRR data.**

### 5.3. Bulk modeling of SHF

In many lakes, SHF is the most important component controlling the lake's energy content. Accurate methods for the determination of SHF are valuable for water management, and for use in hydrological and meteorological models. Large lakes, not surprisingly, are subject to spatially and temporally varying meteorological conditions, and hence SHF. The total SHF is the net effect of five main terms: solar shortwave radiation, atmospheric radiation, surface reflection, evaporation and convection. In this work, we evaluate the contributions of these different factors to the overall SHF.

We evaluated several bulk formulas obtained by different representations of the aforementioned five terms, which led to 64 different surface heat flux models. Data sources to run the models include results of the COSMO-2 model and LSWT from AVHRR satellite imagery. Models are calibrated at two points in the lake for which regular depth profiles of temperature are available, and which enable computation of the total heat content variation,  $G$ . The latter, computed for 03.2008-12.2012, integrated using:

$$G_{obs}(t) = \int_0^H \rho_w C_p T(z, t) dz \quad (1)$$

while the model heat content is the time-integration of the net heat flux for the observation period:

$$G_{mo}(t) = \int_0^t Q_{tot}(t') dt' \quad (2)$$

In the above equations,  $\rho_w$ ,  $C_p$ ,  $T(z, t)$  and  $Q_{tot}$  are water density [ $kg\ m^{-3}$ ], specific heat capacity of water [ $J\ kg^{-1}\ K^{-1}$ ], vertical temperature profiles [ $K$ ] at time  $t$  [ $s$ ] up to depth  $H$  [ $m$ ] and total SHF [ $W\ m^{-2}$ ] respectively.

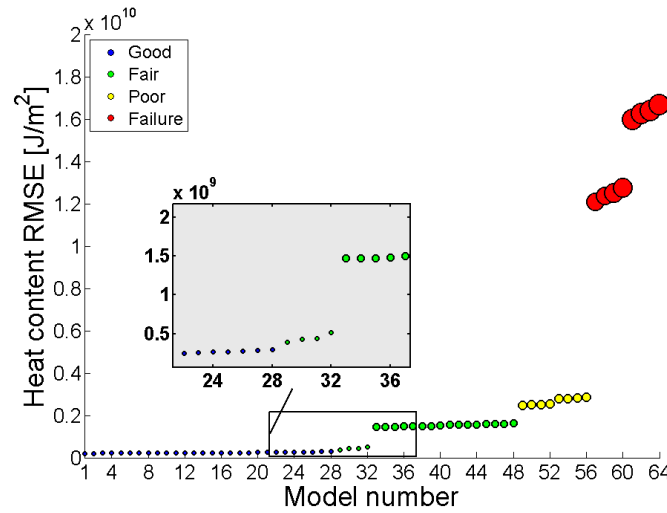
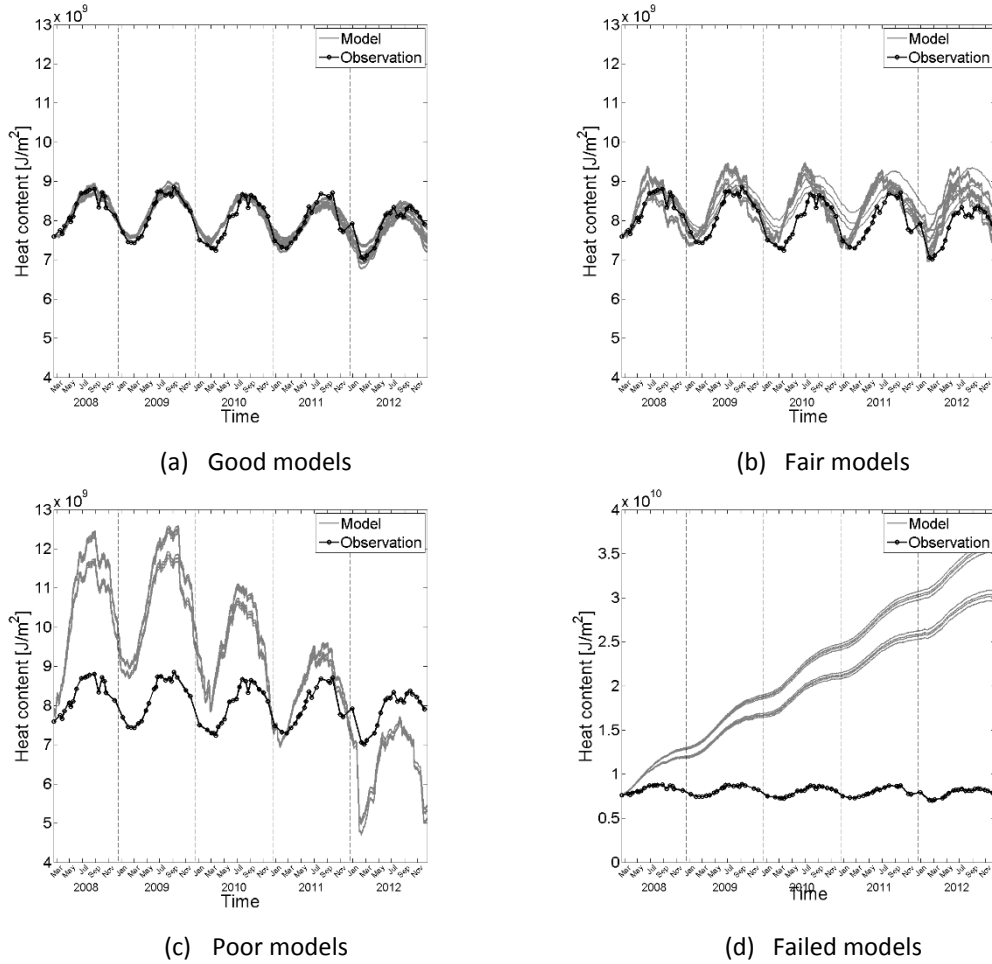


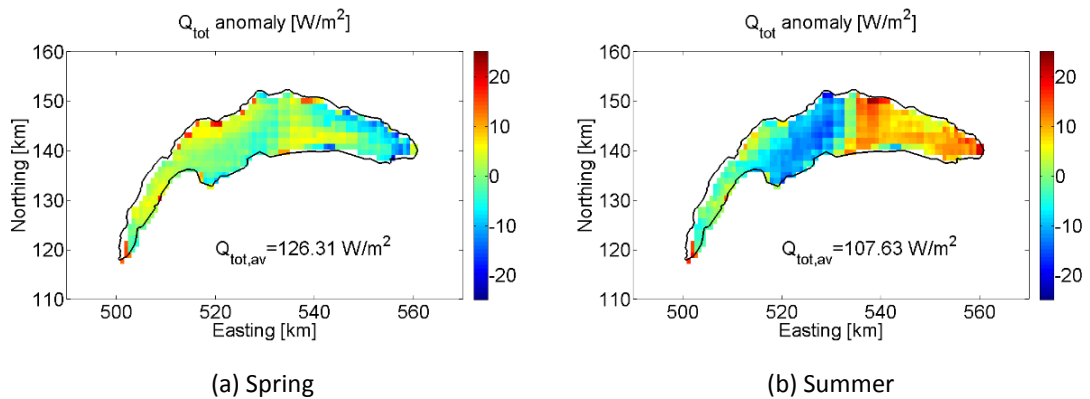
Figure 25: Bulk SHF classification for the selected models

The performance of the SHF models can be classified into four categories as shown in Figure 25. The comparison at one of the calibration points, called SHL2 (coord CH: 534.700/144.950), are also presented in Figure 26. The failed or poor models are mainly due to simplifications in atmospheric radiation and surface reflection terms. The results show that the most critical terms is the evaporative/convective heat flux.



**Figure 26: The models results and monitoring point (SHL2) heat content variation for 2008-2012.**

The best calibrated model was then selected to calculate the spatial distribution of SHF. The seasonal average total heat fluxes together with their spatial variations are shown in Figure 27. The results illustrate that the average net heat input into the lake is higher in the eastern part than in the western. Over the full year, the evaporative heat flux is significant in all seasons while the convective heat flux plays a role mainly in fall and winter. Meteorological observations demonstrate that wind-sheltering, and to some extent relative humidity variability, are the main reasons for the observed large-scale spatial variability. As an example, the average spatial patterns of different SHF terms as well as wind speed over the lake during fall are shown in Figure 28.





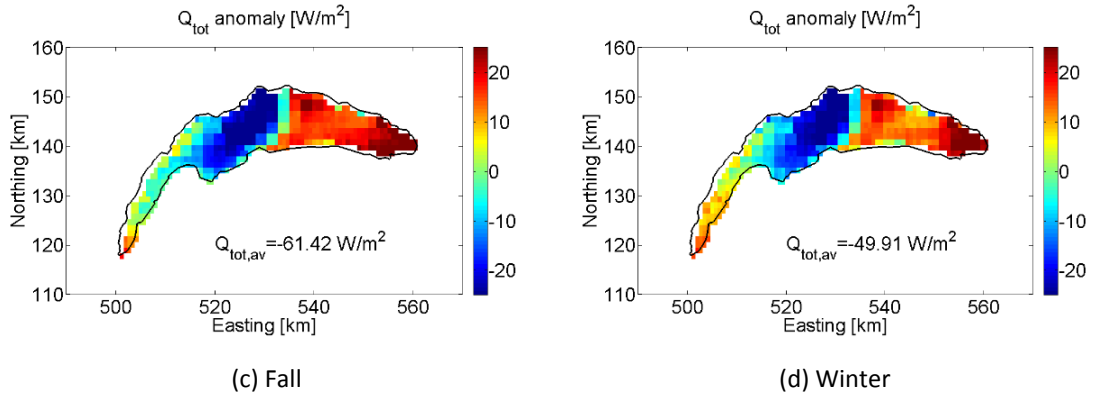
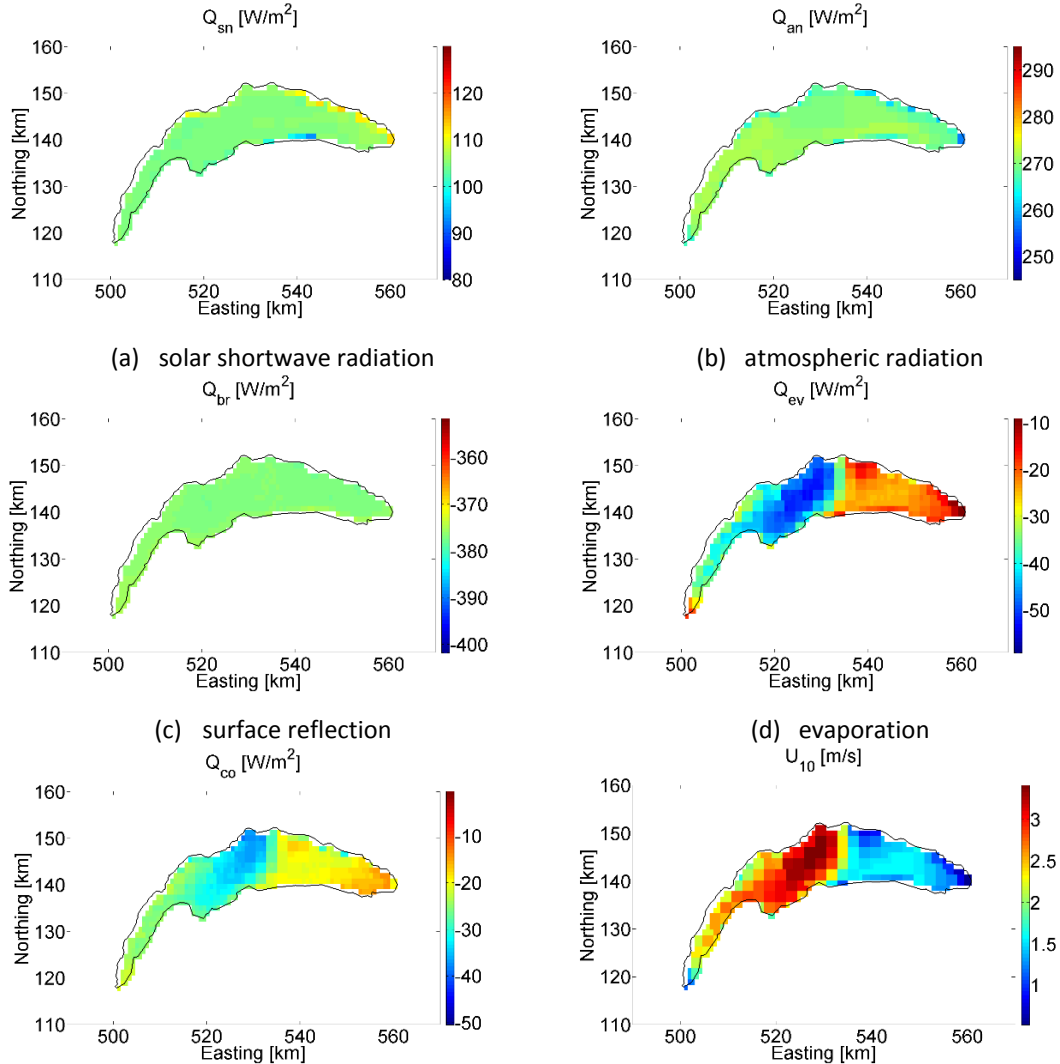


**Figure 27: SHF seasonal average values and their anomalies.**

The model results for all seasons (only fall results are shown in Figure 26) reveal that the radiation SHF terms do not show any spatial variability whereas the spatial variation of evaporation and convection heat fluxes may reach up to  $52 \text{ W/m}^2$  and  $35 \text{ W/m}^2$ , respectively. In addition, both modelling (Figure 27) and satellite observations (Figure 24) indicate that, on average, the eastern part of the lake is warmer than the western part, with a greater temperature contrast in spring and summer than in fall and winter whereas the SHF spatial splitting is stronger in fall and winter. This is mainly due to negative heat flux values (net cooling) and stronger wind forcing, and consequently stronger mixing, in cold seasons.



(e) convection

(f) wind speed at 10 m above the water  
surface

Figure 28: Average SHF terms together with average wind forcing patterns for fall 2008-2012.

#### 5.4. Meso-scale LSWT data acquisition platform

An improved understanding of surface transport processes is necessary to predict sediment, pollutant and phytoplankton patterns in large lakes. These patterns are strongly linked to LSWT as a fundamental component of physical limnology. There are different data sources for LSWT mapping, including remote sensing and in-situ measurements. The available satellite data might be suitable for detecting the large-scale thermal patterns (sections 5.1 and 5.2), but not the meso- or small scale processes. Lake surface thermography, investigated in this study, has finer resolution compared to satellite images. Thermography at the meso-scale provides the ability to ground-truth satellite imagery over scales of one to several satellite image pixels. On the other hand, thermography data can be used as a control in schemes to upscale local measurements that account for the surface energy fluxes and vertical energy budget. Independently, since such data can be collected at high frequency, they can be also useful in capturing the surface signatures of meso-scale eddies and thus to quantify mixing processes. In the present work, we report the preliminary results from the BLIMP system, which was developed for this purpose.

The BLIMP consists of a small balloon which is tethered to a boat and equipped with the thermal and RGB cameras, as well as other instrumentation for location and communication (Figure 29).

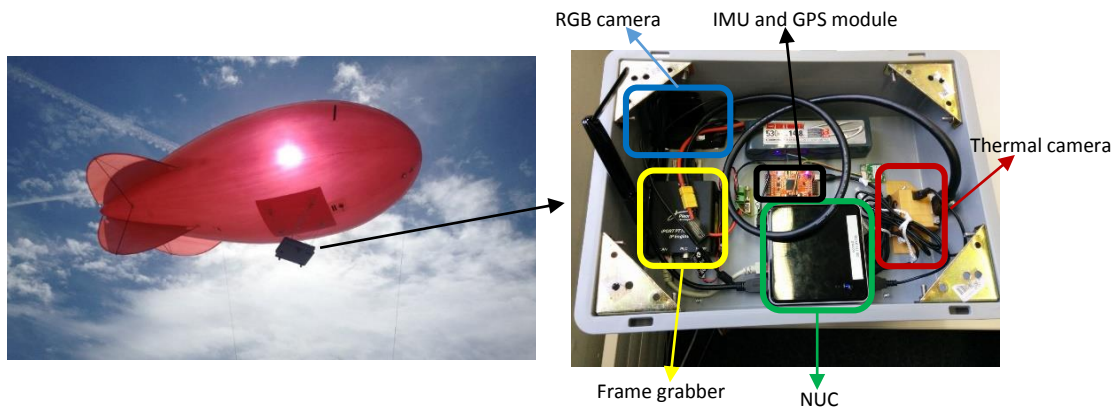
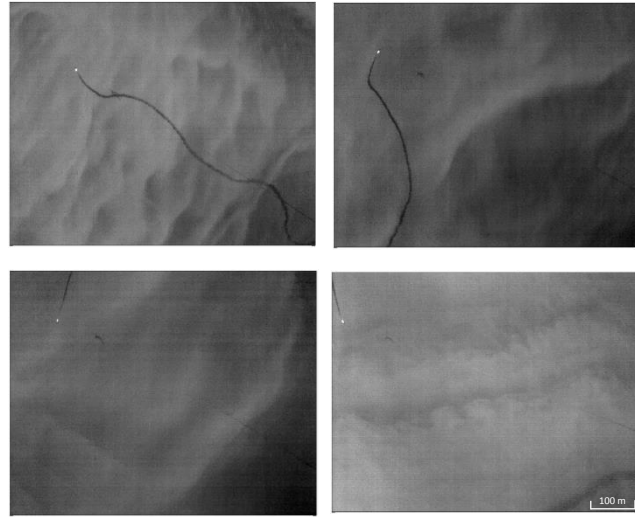


Figure 29: Balloon Launched Imaging and Monitoring Platform (BLIMP) launched on 1<sup>st</sup> July 2015 (left) and instrumentation (right).

In a typical deployment, the BLIMP is towed by the boat, and collects high frequency data from different heights (i.e., spatial resolutions) and locations. One deployment was carried out on Lake Geneva in 2015 of which some thermal images are shown in Figure 30. The field measurement was performed in a calm afternoon in summertime. Since no ground-truthing (radiometric calibration) were carried out, the images represent the 14-bit digital values not the absolute temperature. However, the BLIMP thermography reveals some hydrodynamically-driven structures in the LSWT as well as, not surprisingly, mixing processes due to boat tracks. These patterns are more detectable in the upper-left image in Figure 30b. The main factors driving such thermal patterns will be addressed in this project.



(a) Area tracked by BLIMP on Lake Geneva

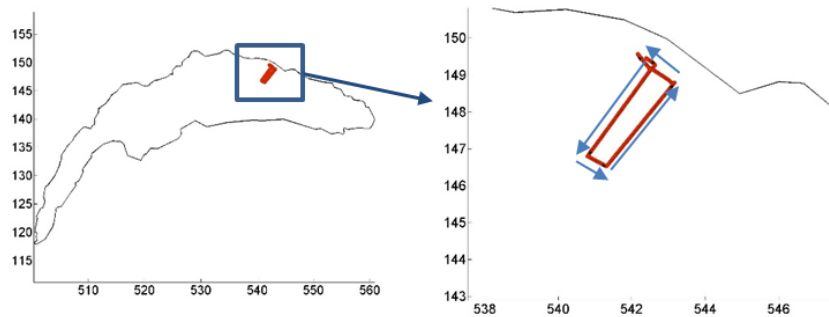


(b) Examples of BLIMP thermography from Lake Geneva.

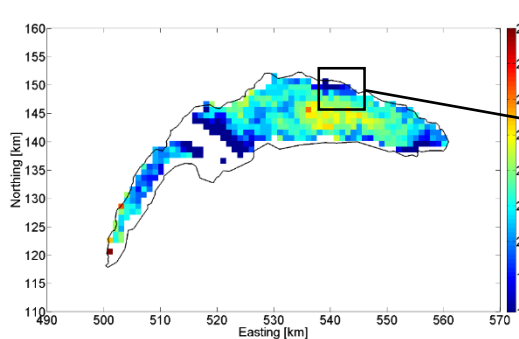
**Figure 30: BLIMP deployment on Lake Geneva, 1 July 2015.**

## 5.5. Outlook

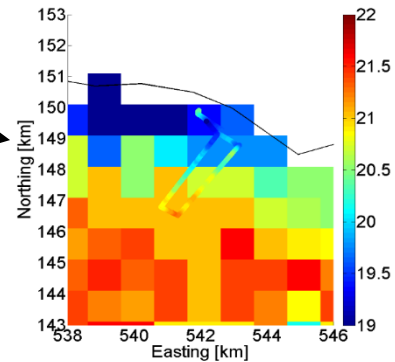
The satellite data, COSMO-2 data and bulk modelling analysis were used to investigate the large-scale thermal variability on Lake Geneva. Some concurrent in situ/BLIMP/satellite measurements are required to ground-truth the satellite data. One campaign, for example, conducted on September 2014 is shown in Figure 31. It reveals a good consistency between the satellite data and in situ LSWT variability.



(a) Autonomous catamaran trajectory on Lake Geneva, 16 September 2014 from 14:15' to 16:19'



(b) NOAA 18 AVHRR overpass at 15:32'



(c) Satellite/in situ temperature comparison

**Figure 31: An example of AVHRR/catamaran data comparison.**

The presented bulk modelling study only uses diurnal AVHRR data. The night-time data will be also added to the current dataset. The methodology explained in section 5.2 will be applied for an extended period, i.e., 03.2008 to 12.2014, in order to calibrate and verify the SHF models. Finally, the diurnal, nocturnal and seasonal surface thermal patterns will be obtained. Then, the dominant factors controlling such large-scale patchiness will be investigated.

One limitation inherent in the bulk models is their inability to consider water transport. A 3D model seems an appropriate tool, although its calibration procedure for a large water body is not straightforward. In this work, the Delft3D hydrodynamic model will be used to simulate Lake Geneva's seasonal thermal structure (see Léman-Baikal annual report 2014 for more details on the model). Then, a statistical method, e.g., empirical orthogonal functions (EOF), will be used to find the dominant thermal, meteorological and hydrodynamic patterns. The links between these patterns will be examined in the context of the different physical mechanisms involved, thereby providing insights into the variability of the LSWT and SHF in a large lake.

Regarding the meso-scale LSWT investigation, simultaneous ground-truthing of the BLIMP data is required using an autonomous craft that collects a variety of data, including in situ surface/near surface temperatures, currents, radiation and meteorological data in the area covered by the BLIMP images. The ECOL catamaran, with a portable acoustic Doppler current profiler (ADCP) mounted on the current configuration, will be used for this purpose. The perspective is to cover at least two zones, one in the eastern part of the lake and one in the middle/western part, in different seasons.

## 6. Princeton effort in collaboration with EFLUM/CRYOS

Prof. M Hultmark, G. Arwatz, Dr. H Huwald and Prof. M B Parlange

### 6.1. Objective

The goal for the Princeton part of this effort was to develop an ultra-fast-response temperature and humidity sensors. A temperature sensor, several orders of magnitude faster than conventional sensors, has been developed, tested and utilized in laboratory studies. The temperature sensor was used on the ULM, but due to problems with the GPS, simultaneous position data is not available. A humidity sensor has also been developed and manufactured, and is currently in the evaluation stage.

These sensors are designed to enable unprecedented investigations of the full range of turbulent scales present in the atmospheric boundary layer. In combination with velocity measurements an accurate estimate of the latent heat and sensible heat flux from the surface can be made. Additionally, the turbulent humidity, temperature spectrum and their co-spectrum can be calculated and compared to existing models.

### 6.2. Sensor development

When relating the heat transfer from a nano-wire to the humidity knowing the instantaneous temperature is crucial. Early in the development stage of the humidity sensor, it was observed that the state of the art temperature sensors were much slower than previously believed. Thus, in order to successfully design a humidity sensor, we had to first develop a fast response temperature sensor.

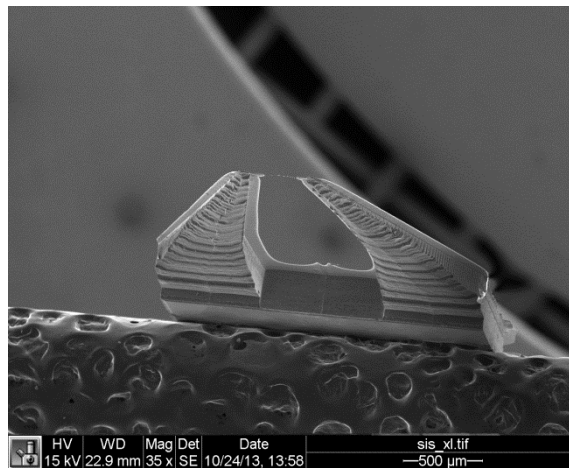


Figure 32: MEMS temperature sensor (T-NSTAP)

Conventionally, cold-wires are used to measure turbulent temperature fluctuations. However, while characterizing them using a chopped laser system, it was noticed that their frequency response was more than two orders of magnitude slower than previously believed. To explain this observation, a lumped capacitance model of the dynamics of cold-wires was developed (Arwatz et al., 2013). This model can be used to correct data taken with conventional sensors, or it can be used to design an improved temperature sensor. We chose the latter approach due to its robustness. A MEMS-based temperature sensor has been successfully manufactured (T-NSTAP, Figure 32) using techniques previously developed for a velocity sensors (NSTAP). The design of the T-NSTAP is such that it minimized end-conduction effects, and thus minimizes low frequency attenuation of the

measured temperature signal. By making the wire very thin, the thermal mass can be kept low to improve the high frequency behaviour. A test bench was built, in addition to the laser test, consisting of an alternating hot and cold jet which allows us to study the frequency response of the T-NSTAP (Figure 33). The results indicate that the new sensors are several orders of magnitude faster than conventional cold-wires. A detailed description of the T-NSTAP and the comparison to conventional cold-wires can be found in Arwatz et al. (2015).

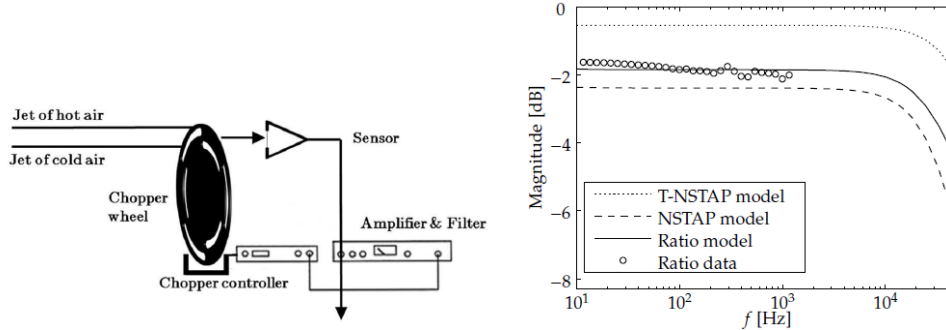


Figure 33: Schematic of test setup and resulting Bode plot

With a substantially improved temperature sensor, the work on the humidity sensor has resumed. In order to measure fast-response humidity we have been developing a brand new sensor based on a previously unexplored principle. The Peclet number is the ratio of the heat transfer due to convection over that due to molecular diffusion and is defined as  $Pe = \frac{LU}{\alpha}$ , (where  $L$  is the diameter of the wire,  $U$  the velocity over it and  $\alpha$  the thermal diffusivity of the air). Thus, a small Peclet number implies that molecular diffusion is dominating. This effect is explored in our sensor to relate molecular diffusion, which is a strong function of humidity. To reduce the Peclet number, the length scale,  $L$ , is decreased by using a nano-wire as heating element. The small characteristic length scale of the wire results in a Peclet number less than unity. This allows us to reduce the sensitivity to velocity and make a sensor that is mainly sensitive to thermal conductivity of the surrounding fluid.

In order to reduce the Peclet number, a sensor was manufactured consisting of a 10  $\mu\text{m}$  long free-standing Platinum wire with 120 x 500 nm cross-section. The sensor is deposited on a silicon wafer with a silicone oxide layer. The minute scale of the wire posed new problems, since the internal stresses in the silicone oxide broke the wire when released. To overcome this issue we have developed a new method with layers of silicon oxide and silicon nitride that results in internal stresses an order of magnitude smaller than the oxide alone. This allowed us to successfully manufacture the sensor with a free standing platinum nano-wire.

The new humidity sensor is operated using a constant temperature feedback circuit. However, none of the commercially available systems were able to operate the new sensor due to either over current or instabilities, with immediate and catastrophic failure as result. Therefore, a custom-built circuit was developed with reduced current and increased adjustments of the feedback characteristics, to avoid oscillations. After many attempts a circuit was built that successfully can operate the new sensor in a stable configuration. Due to the miniscule thermal mass of the wire, it can adapt to a change in the environment much faster than any sensor available. By exposing the sensor to a square wave in the current and observing the response its bandwidth can be approximated. The resulting response is shown in Figure 34, with a bandwidth close to 0.5 Mhz. This is almost 5 orders of magnitude



faster than conventional humidity sensors. The accuracy and sensitivity of the new sensor is currently being evaluated.

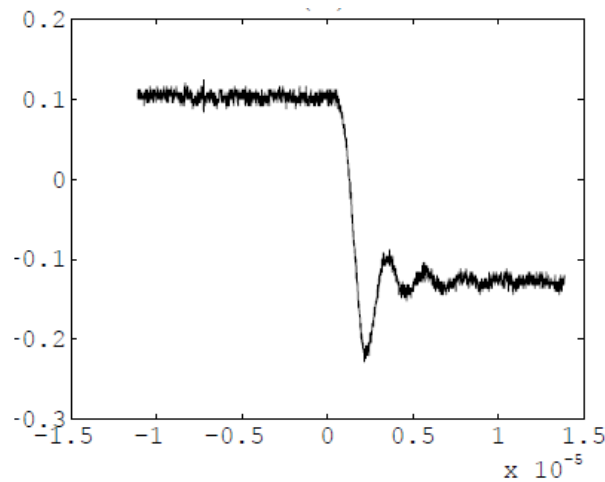


Figure 34: Square-wave test of the q-NSTAP sensor indicating close to 0.5 MHz frequency response.

### 6.3. Field experiments

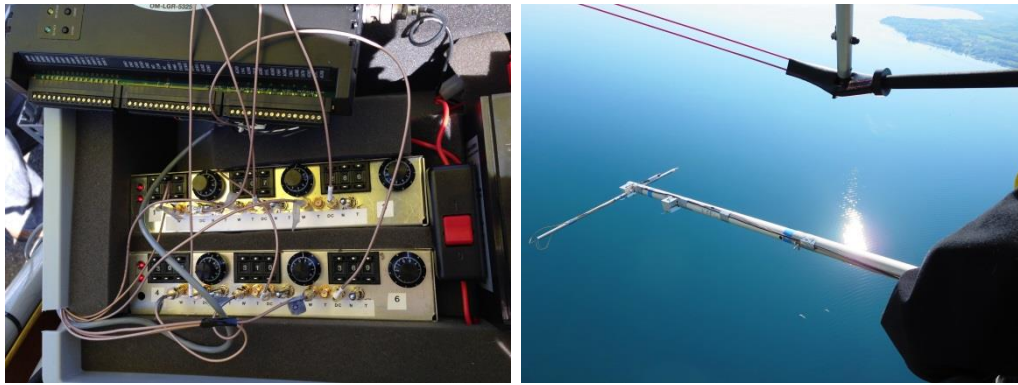
An experimental investigation to assess the feasibility of using nano-scale temperature sensors on the ULMs was carried out in a series of tests above Lake Geneva. The new sensor had shown superior performance when compared to traditional cold wires in laboratory setting. However, the ultimate goal of the current study is to measure with the sensors over Lake Geneva, mounted to the ULM. The combination of these measurements with velocity and position measurements by other groups guarantees unfiltered atmospheric data. To test the reliability in the field 6 nano-scale probes were installed on each side of a ULM's fuselage (as shown in Figure 35).



Figure 35: T-NSTAPs mounted on the side of the ULM fuselage.

Temperature data was acquired using specially designed constant current circuit (designed and built at Princeton University). The circuit is designed for low noise level and low sensitivity to ambient conditions. The autonomous data acquisition was installed on the ULM to acquire data during flight (as seen in Figure 36).





**Figure 37 (a) On-board integration of the data acquisition and (b) the sensors during flight.**

It was shown that the sensor performed well during various flight conditions. The sensors survived takeoff, landing and cruising at velocities up to 25 m/s. Due to lack of telemetry (GPS altitude and velocity) on the ULM at the time of tests, temperature data is of limited use. However, the feasibility and robustness of the sensors were tested and validated with great success.

## 7. Reference

- Arwatz G, Bahri C, Smits A J and Hultmark M. (2013): Dynamic calibration and modeling of a cold wire for temperature measurement. *Measurement Science and Technology* (24): 125301. doi:10.1088/0957-0233/24/12/125301
- Arwatz G, Fan Y, Bahri C and Hultmark M. (2015): Development and characterization of a nano-scale temperature probe (T-NSTAP) for turbulent temperature measurement, *Measurement Science and Technology* (26): 035103. doi:10.1088/0957-0233/26/3/035103
- Cubero-Castan M, Constantin D, Barbieux K, Nouchi V, Akhtman Y, and Merminod B (2015): A new smoothness based strategy for semi-supervised atmospheric correction: application to the Leman-Baikal campaign. In 7th Workshop on Hyperspectral Image and Signal Processing: Evolution in Remote Sensing, number EPFL-CONF- 207776.
- Tarasov M, Shinkareva G, Tutubalina O, Lychagin M, Constantin D, Rehak M, Yosef Akhtman Y, Merminod B, Tofield-Pasche N, Chalov S et al.(2015) Investigation of heavy metals distribution in suspended matter and macrophytes of the Selenga river delta using airborne hyperspectral remote sensing. In 9th EARSeL SIG Imaging Spectroscopy workshop, number EPFL-POSTER-207767.
- Triggs B, McLauchlan P F, Hartley R I, and Fitzgibbon A B (2000): Bundle adjustment: a modern synthesis. In *Vision algorithms: theory and practice*, pages 298–372. Springer.